

29. Cosmic Microwave Background

Revised August 2023 by D. Scott (U. of British Columbia) and G.F. Smoot (HKUST; UC Berkeley; LBNL; DIPC; Paris U.).

29.1 Introduction

The energy content in electromagnetic radiation from beyond our Galaxy is dominated by the cosmic microwave background (CMB), discovered in 1965 [1]. Its spectral distribution is well described by a blackbody function with $T = 2.7255\text{ K}$, which is a principal pillar of the hot Big Bang model for the Universe, with the lack of any observed deviations from a Planckian spectrum constraining physical processes over cosmic history at redshifts $z \lesssim 10^7$ (see earlier versions of this review).

The key information in the CMB sky is extracted from the observed angular variation of its temperature (or intensity) correlations, and to a growing extent polarization [2]. After the first detection of CMB anisotropies by the Cosmic Background Explorer (*COBE*) satellite in 1992 [3], there has been intense activity to map the sky at increasing levels of sensitivity and angular resolution by ground-based and balloon-borne measurements. These were joined in 2003 by the first results from NASA's Wilkinson Microwave Anisotropy Probe (*WMAP*) [4], which were improved upon by analyses of data added every 2 years, culminating in the 9-year results [5]. In 2013 we had the first results [6] from the third generation CMB satellite, ESA's *Planck* mission [7], which were enhanced by results from the 2015 *Planck* data release [8, 9], and then the final 2018 *Planck* data release [10, 11]. Additionally, CMB anisotropies have been extended to smaller angular scales by ground-based experiments, particularly the Atacama Cosmology Telescope (ACT) [12] and the South Pole Telescope (SPT) [13]. Together these observations have led to a stunning confirmation of the ‘Standard Model of Cosmology.’ In combination with other astrophysical data, the CMB anisotropy measurements place quite precise constraints on a number of cosmological parameters, and have launched us into an era of precision cosmology. With more than half a century of study of the CMB, the program to map temperature anisotropies is effectively wrapping up, and attention is increasingly focussing on polarization measurements, which promise further tests of fundamental physics.

29.2 CMB Spectrum

It is well-known that the spectrum of the microwave background is very precisely that of black-body radiation, whose temperature evolves with redshift as $T(z) = T_0(1 + z)$ in an expanding Universe. As a direct confirmation of its cosmological origin, this relationship has been tested by measuring the strengths of emission and absorption lines in high-redshift systems (*e.g.*, Ref. [14]).

Measurements of the spectrum are consistent with a blackbody distribution over more than three decades in frequency (there is a claim by ARCADE [15] of a possible unexpected extragalactic emission signal at low frequency, but the interpretation is debated [16]). All viable cosmological models predict a very nearly Planckian spectrum to within the current observational limits. Because of this, measurements of deviations from a blackbody spectrum have received little attention in recent years, with only a few exceptions. However, that situation will likely change as proposed experiments [17] are built that have the potential to dramatically improve early Universe energy release constraints. It now seems feasible to probe spectral distortion mechanisms that are *required* in the standard picture, such as those arising from the damping and dissipation of relatively small-scale primordial perturbations, or the average effect of inverse Compton scattering. A more ambitious goal would be to reach the precision needed to detect the residual lines from the cosmological recombination of hydrogen and helium and hence to test whether conditions at $z \gtrsim 1000$

accurately follow those in the standard picture [18].

29.3 Description of CMB Anisotropies

Observations show that the CMB contains temperature anisotropies at the 10^{-5} level and polarization anisotropies at the 10^{-6} (and lower) level, over a wide range of angular scales. These anisotropies are usually expressed using a spherical harmonic expansion of the CMB sky:

$$T(\theta, \phi) = \sum_{\ell m} a_{\ell m} Y_{\ell m}(\theta, \phi) \quad (29.1)$$

(with the linear polarization pattern written in a similar way using the so-called spin-2 spherical harmonics). Increasing angular resolution requires that the expansion goes to higher multipoles. Because only very weak phase correlations are observed in the CMB sky and no preferred direction is seen, the vast majority of the cosmological information is found in the temperature 2-point function, *i.e.*, the variance as a function only of angular separation. Equivalently, the anisotropy power per unit $\ln \ell$ is $\ell \sum_m |a_{\ell m}|^2 / 4\pi$.

29.3.1 The Monopole

The CMB has a mean temperature of $T_\gamma = 2.7255 \pm 0.0006$ K (1σ) [19], which can be considered as the monopole component of CMB maps, a_{00} . Because all mapping experiments involve difference measurements, they are insensitive to this average level; monopole measurements can only be made with absolute temperature devices, such as the FIRAS instrument on the *COBE* satellite [20]. The measured kT_γ is equivalent to 0.234 meV or $4.60 \times 10^{-10} m_e c^2$. A blackbody of the measured temperature has a number density $n_\gamma = (2\zeta(3)/\pi^2) T_\gamma^3 \simeq 411 \text{ cm}^{-3}$, energy density $\rho_\gamma = (\pi^2/15) T_\gamma^4 \simeq 4.64 \times 10^{-34} \text{ g cm}^{-3} \simeq 0.260 \text{ eV cm}^{-3}$, and a fraction of the critical density $\Omega_\gamma \simeq 5.38 \times 10^{-5}$.

29.3.2 The Dipole

The largest anisotropy is in the $\ell = 1$ (dipole) first spherical harmonic, with amplitude 3.3621 ± 0.0010 mK [10]. The dipole is interpreted to be the result of the Doppler boosting of the monopole caused by the Solar System motion relative to the nearly isotropic blackbody field, as broadly confirmed by measurements of the radial velocities of local galaxies (*e.g.*, Ref. [21]); the intrinsic (non-Doppler) part of the signal is expected to be 2 orders of magnitude smaller (and fundamentally difficult to distinguish). The motion of an observer with velocity $\beta \equiv v/c$ relative to an isotropic Planckian radiation field of temperature T_0 produces a Lorentz-boosted temperature pattern

$$\begin{aligned} T(\theta) &= T_0(1 - \beta^2)^{1/2} / (1 - \beta \cos \theta) \\ &\simeq T_0 \left[1 + \beta \cos \theta + \left(\beta^2/2 \right) \cos 2\theta + O(\beta^3) \right]. \end{aligned} \quad (29.2)$$

At every point in the sky, one observes a blackbody spectrum, with temperature $T(\theta)$. The spectrum of the dipole has been confirmed to be the differential of a blackbody spectrum [22]. At higher order there are additional effects arising from aberration and from modulation of the anisotropy pattern, which have also been observed [23].

The implied velocity for the Solar System barycenter is $v = 369.82 \pm 0.11 \text{ km s}^{-1}$, assuming a value $T_0 = T_\gamma$, towards $(l, b) = (264.021^\circ \pm 0.011^\circ, 48.253^\circ \pm 0.005^\circ)$ [10]. This Solar System motion implies a velocity for the Galaxy and the Local Group of galaxies relative to the CMB of $v_{LG} = 620 \pm 15 \text{ km s}^{-1}$ towards $(l, b) = (271.9^\circ \pm 2.0^\circ, 29.6^\circ \pm 1.4^\circ)$ [10]; most of the error comes from uncertainty in the velocity of the Solar System relative to the Local Group.

The dipole is a frame-dependent quantity, and one can thus determine the ‘CMB frame’ (*in some sense this is a special frame*) as that in which the CMB dipole would be zero. Any velocity of

the receiver relative to the Earth and the Earth around the Sun is removed for the purposes of CMB anisotropy studies, while our velocity relative to the Local Group of galaxies and the Local Group's motion relative to the CMB frame are normally removed for cosmological studies. The dipole is now routinely used as a primary calibrator for mapping experiments, either via the time-varying orbital motion of the Earth, or through the cosmological dipole measured by satellite experiments.

29.3.3 Higher-Order Multipoles

The variations in the CMB temperature maps at higher multipoles ($\ell \geq 2$) are interpreted as being mostly the result of density perturbations in the early Universe, manifesting themselves at the epoch of the last scattering of the CMB photons. In the hot Big Bang picture, the expansion of the Universe cools the plasma so that by a redshift $z \simeq 1100$ (with little dependence on the details of the model), the hydrogen and helium nuclei can bind electrons into neutral atoms, a process usually referred to as ‘recombination’ [24]. Before this epoch, the CMB photons were tightly coupled to the charged baryons, while afterwards they could freely stream towards us. By measuring the $a_{\ell m}$ s we are thus learning directly about physical conditions in the early Universe.

A statistically-isotropic sky means that all m s are equivalent, *i.e.*, there is no preferred axis, so that the temperature correlation function between two positions on the sky depends only on angular separation and not orientation. Together with the assumption of Gaussian statistics (*i.e.*, no correlations between the modes), the 2-point function of the temperature field (or equivalently the power spectrum in ℓ) then fully characterizes the anisotropies. The power summed over all m s at each ℓ is $(2\ell + 1)C_\ell/(4\pi)$, where $C_\ell \equiv \langle |a_{\ell m}|^2 \rangle$. Thus, averages of $a_{\ell m}$ s over m can be used as estimators of the C_ℓ s to constrain their expectation values, which are the quantities predicted by a theoretical model. For an idealized full-sky observation, the variance of each measured C_ℓ (*i.e.*, the variance of the variance) is $[2/(2\ell + 1)]C_\ell^2$. This sampling uncertainty (known as ‘cosmic variance’) comes about because each C_ℓ is χ^2 distributed with $(2\ell + 1)$ degrees of freedom for our observable volume of the Universe. For fractional sky coverage, f_{sky} , this variance is increased by $1/f_{\text{sky}}$ and the modes become partially correlated.

It is important to understand that theories predict the expectation value of the power spectrum, whereas our sky is a *single* realization. Hence, the cosmic variance is an unavoidable source of uncertainty when constraining models; it dominates the scatter at lower ℓ s, while the effects of instrumental noise and resolution dominate at higher ℓ s [25].

Theoretical models generally predict that the $a_{\ell m}$ modes are Gaussian random fields to high precision, matching the empirical tests, *e.g.*, standard slow-roll inflation’s non-Gaussian contribution is expected to be at least an order of magnitude below current observational limits [26]. Although non-Gaussianity of various forms is possible in early Universe models, tests show that Gaussianity is an extremely good simplifying approximation [27]. The only current indications of any non-Gaussianity or statistical anisotropy are some relatively weak signatures at large scales, seen in both *WMAP* [28] and *Planck* data [29], but not of high enough significance to reject the simplifying assumption. Nevertheless, models that deviate from the inflationary slow-roll conditions can have measurable non-Gaussian signatures. So while the current observational limits make the power spectrum the dominant probe of cosmology, it is worth noting that higher-order correlations are tools for constraining otherwise viable theories.

29.3.4 Angular Resolution and Binning

There is no one-to-one conversion between multipole ℓ and the angle subtended by a particular spatial scale projected onto the sky. However, crudely speaking, a single spherical harmonic $Y_{\ell m}$ corresponds to angular variations of $\theta \sim \pi/\ell$. CMB maps contain anisotropy information from the size of the map (or in practice some fraction of that size) down to the beam-size of the instrument, σ (the standard deviation of the beam, in radians). One can think of the effect of a Gaussian beam

as rolling off the power spectrum with the function $e^{-\ell(\ell+1)\sigma^2}$.

For less than full sky coverage, the ℓ modes become correlated. Hence, experimental results are usually quoted as a series of ‘band powers,’ defined as estimators of $\ell(\ell+1)C_\ell/2\pi$ over different ranges of ℓ . Because of the strong foreground signals in the Galactic plane, even ‘all-sky’ surveys, such as *WMAP* and *Planck*, involve a cut sky. The amount of binning required to obtain uncorrelated estimates of power also depends on the map size.

29.4 Cosmological Parameters

The current ‘Standard Model’ of cosmology contains around 10 free parameters, only six of which are required to have non-null values (see The Cosmological Parameters—Sec. 25 of this *Review*). The basic framework is the Friedmann-Robertson-Walker (FRW) metric (*i.e.*, a Universe that is approximately homogeneous and isotropic on large scales), with density perturbations laid down at early times and evolving into today’s structures (see Big-Bang cosmology—Sec. 22 of this *Review*). The most general possible set of density variations is a linear combination of an adiabatic density perturbation and some isocurvature perturbations. Adiabatic means that there is no change to the entropy per particle for each species, *i.e.*, $\delta\rho/\rho$ for matter is $(3/4)\delta\rho/\rho$ for radiation. Isocurvature means that the set of individual density perturbations adds to zero, for example, matter perturbations compensate radiation perturbations so that the total energy density remains unperturbed, *i.e.*, $\delta\rho$ for matter is $-\delta\rho$ for radiation. These different modes give rise to distinct (temporal) phases during growth, with those of the adiabatic scenario being fully consistent with the data. Models that generate mainly isocurvature type perturbations (such as most topological defect scenarios) are not viable. However, an admixture of the adiabatic mode with up to 1.7% isocurvature contribution (depending on details of the mode) is still allowed [30].

29.4.1 Initial Condition Parameters

Within the adiabatic family of models, there is, in principle, a free function describing the variation of comoving curvature perturbations, $\mathcal{R}(\mathbf{x}, t)$. The great virtue of \mathcal{R} is that it is constant in time on super-horizon scales for a purely adiabatic perturbation. There are physical reasons to anticipate that the variance of these perturbations will be described well by a power law in scale, *i.e.*, in Fourier space $\langle|\mathcal{R}|_k^2\rangle \propto k^{n_s-4}$, where k is wavenumber and n_s is the spectral index as usually defined. So-called ‘scale-invariant’ initial conditions (meaning gravitational potential fluctuations that are independent of k) correspond to $n_s = 1$. In inflationary models [31] (see Inflation—Sec. 23 of this *Review*), perturbations are generated by quantum fluctuations, which are set by the energy scale of inflation together with the slope and higher derivatives of the inflationary potential. One generally expects that the Taylor series expansion of $\ln \mathcal{R}_k(\ln k)$ has terms of steadily decreasing size. For the simplest models, there are thus two parameters describing the initial conditions for density perturbations, namely the amplitude and slope of the power spectrum. These can be explicitly defined, for example, through

$$\mathcal{P}_{\mathcal{R}}^2 \equiv k^3 \langle |\mathcal{R}|_k^2 \rangle / 2\pi^2 \simeq A_s (k/k_0)^{n_s-1}, \quad (29.3)$$

with $A_s \equiv \mathcal{P}_{\mathcal{R}}^2(k_0)$ and $k_0 = 0.05 \text{ Mpc}^{-1}$, say. There are other equally valid definitions of the amplitude parameter (see also Secs. 22, 23, and 25 of this *Review*), and we caution that the relationships between some of them can be cosmology-dependent. In slow-roll inflationary models, this normalization is proportional to the combination $V^3/(V')^2$, for the inflationary potential $V(\phi)$. The slope n_s also involves V'' , and so the combination of A_s and n_s can constrain potentials.

Inflation generates tensor (gravitational wave) modes, as well as scalar (density perturbation) modes. This property introduces another parameter, measuring the amplitude of a possible tensor component, or equivalently the ratio of the tensor to scalar contributions. The tensor amplitude is

$A_t \propto V$, and thus one expects a larger gravitational wave contribution in models where inflation happens at higher energies. The tensor power spectrum also has a slope, often denoted n_t , but since this seems unlikely to be measured in the near future (and there is also a consistency relation with tensor amplitude), it is sufficient for now to focus only on the amplitude of the gravitational wave component. It is most common to define the tensor contribution through r , the ratio of tensor to scalar perturbation spectra at some fixed value of k (e.g., $k = 0.002 \text{ Mpc}^{-1}$ or $k = 0.05 \text{ Mpc}^{-1}$, although it was historically defined in terms of the ratio of contributions at $\ell = 2$). Different inflationary potentials will lead to different predictions, e.g., for 50 e-folds, $\lambda\phi^4$ inflation gives $r = 0.32$ and $m^2\phi^2$ inflation gives $r = 0.16$ (both now strongly disfavored by the data), while other models can have arbitrarily small values of r . In any case, whatever the specific definition, and whether they come from inflation or something else, the ‘initial conditions’ give rise to a minimum of three parameters, A_s , n_s , and r .

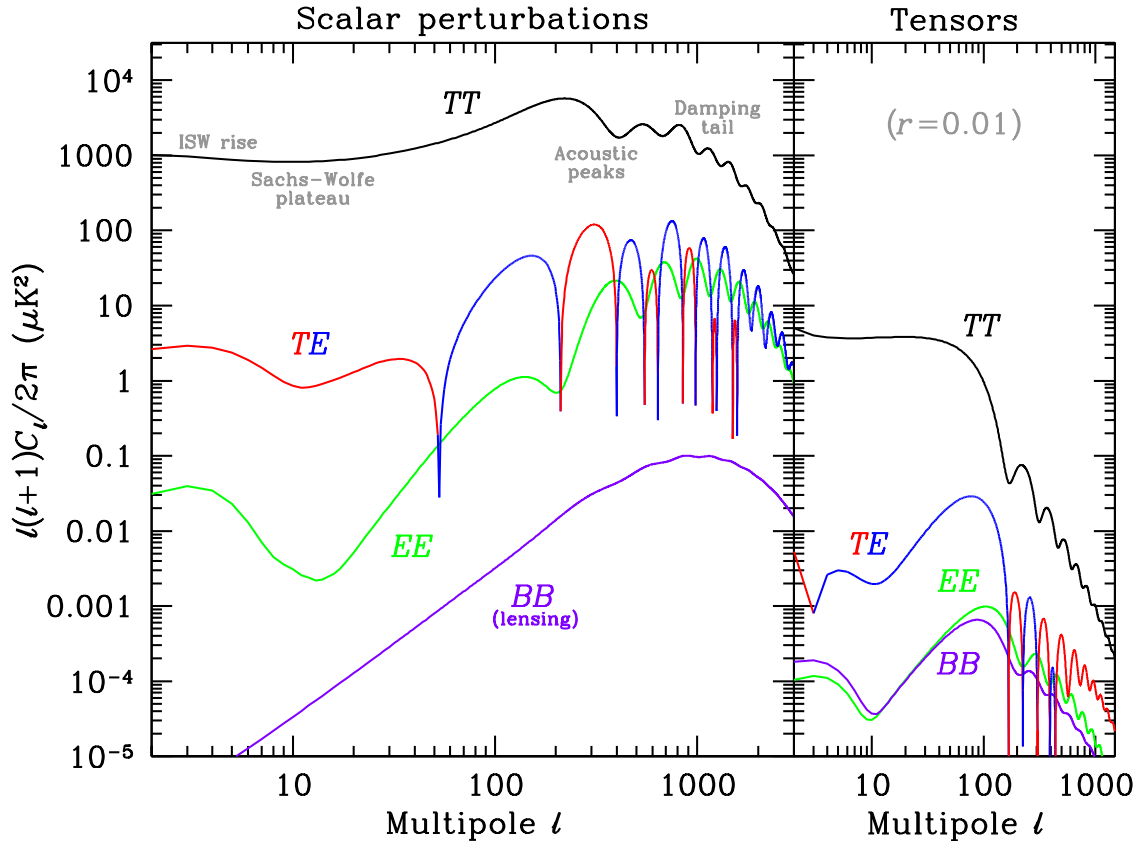


Figure 29.1: Theoretical CMB anisotropy power spectra, using the best-fitting ΛCDM model from *Planck*, calculated using *CAMB*. The panel on the left shows the theoretical expectation for scalar perturbations, while the panel on the right is for tensor perturbations, with an amplitude set to $r = 0.01$ for illustration. Note that the horizontal axis is logarithmic here. For the well-measured scalar TT spectrum, these regions, each covering roughly a decade in ℓ , are labeled as in the text: the ISW rise; Sachs-Wolfe plateau; acoustic peaks; and damping tail. The TE cross-correlation power spectrum changes sign, indicated here by plotting the absolute value, but switching color for the negative parts.

29.4.2 Background Cosmology Parameters

The FRW cosmology requires an expansion parameter (the Hubble constant, H_0 , often represented through $H_0 = 100 h \text{ km s}^{-1} \text{Mpc}^{-1}$) and several parameters to describe the matter and energy content of the Universe. These are usually given in terms of the critical density, *i.e.*, for species ‘x,’ $\Omega_x \equiv \rho_x/\rho_{\text{crit}}$, where $\rho_{\text{crit}} \equiv 3H_0^2/8\pi G$. Since physical densities $\rho_x \propto \Omega_x h^2 \equiv \omega_x$ are what govern the physics of the CMB anisotropies, it is these ω s that are best constrained by CMB data. In particular, CMB observations constrain $\Omega_b h^2$ for baryons and $\Omega_c h^2$ for cold dark matter (with $\rho_m = \rho_c + \rho_b$ for the matter sum).

The contribution of a cosmological constant Λ (or other form of dark energy, see Dark Energy—Sec. 28) is usually included, together with a parameter that quantifies the curvature, $\Omega_K \equiv 1 - \Omega_{\text{tot}}$, where $\Omega_{\text{tot}} = \Omega_m + \Omega_\Lambda$. The radiation content, while in principle a free parameter, is precisely enough determined by the measurement of T_γ that it can be considered fixed, making a $< 10^{-4}$ contribution to Ω_{tot} today.

Astrophysical processes at relatively low redshift can also affect the C_ℓ s, with a particularly significant influence during reionization. The Universe became reionized at some redshift z_i , long after recombination, affecting the CMB when it passed through the integrated Thomson-scattering optical depth:

$$\tau = \int_0^{z_i} \sigma_T n_e(z) \frac{dt}{dz} dz, \quad (29.4)$$

where σ_T is the Thomson cross-section, $n_e(z)$ is the number density of free electrons (which depends on astrophysics), and dt/dz is fixed by the background cosmology. In principle, τ could be determined from the small-scale matter power spectrum, together with the physics of structure formation and radiative feedback processes; however, because this is a sufficiently intractable calculation, in practice τ needs to be considered as a free parameter.

Thus, we have eight basic cosmological parameters, namely A_s , n_s , r , h , $\Omega_b h^2$, $\Omega_c h^2$, Ω_{tot} , and τ . One can add additional parameters to this list, particularly when using the CMB in combination with other data sets. The next most relevant ones might be: $\Omega_\nu h^2$, the massive neutrino contribution; w ($\equiv p/\rho$), the equation of state parameter for the dark energy; and $dn_s/d\ln k$, measuring deviations from a constant spectral index. To these 11 one could of course add further parameters describing additional physics, such as details of the reionization process, features in the initial power spectrum, a sub-dominant contribution of isocurvature modes, *etc.*

As well as these underlying parameters, there are other (dependent) quantities that can be obtained from them. Such derived parameters include the actual Ω s of the various components (*e.g.*, Ω_m), the variance of density perturbations at particular scales (*e.g.*, σ_8), the angular scale of the sound horizon (θ_*), the age of the Universe today (t_0), the age of the Universe at recombination, reionization, *etc.* (see The Cosmological Parameters—Sec. 25).

29.5 Physics of Anisotropies

The cosmological parameters affect the anisotropies through the well understood physics of the evolution of linear perturbations within a background FRW cosmology. There are very effective, fast, and publicly-available software codes for computing the CMB temperature, polarization, and matter power spectra, *e.g.*, CMBFAST [32], CAMB [33], and CLASS [34]. These have been tested over a wide range of cosmologies and are considered to be accurate to much better than the 1% level [35], so that numerical errors are less than 10% of the parameter uncertainties for *Planck* [6].

For pedagogical purposes, it is easiest to focus on the temperature anisotropies, before moving to the polarization power spectra. A description of the physics underlying the C_ℓ^{TT} s can be separated into four main regions (the first two combined below), as shown in the top left part of Fig. 29.1.

29.5.1 The ISW Rise, $\ell \lesssim 10$, and Sachs-Wolfe Plateau, $10 \lesssim \ell \lesssim 100$

The horizon scale (or more precisely, the angle subtended by the Hubble radius) at last scattering corresponds to $\ell \simeq 100$. Anisotropies at larger scales have not evolved significantly, and hence directly reflect the ‘initial conditions.’ Temperature variations are $\delta T/T = -(1/5)\mathcal{R}(\mathbf{x}_{\text{LSS}}) \simeq (1/3)\delta\phi/c^2$, where $\delta\phi$ is the perturbation to the gravitational potential, evaluated on the last-scattering surface (LSS). This is a result of the combination of gravitational redshift and intrinsic temperature fluctuations, and is usually referred to as the Sachs-Wolfe effect [36].

Assuming that a nearly scale-invariant spectrum of curvature (and corresponding density) perturbations was laid down at early times (*i.e.*, $n_s \simeq 1$, meaning equal power per decade in k), then $\ell(\ell+1)C_\ell \simeq \text{constant}$ at low ℓ s. This predicted near-flatness is hard to see unless the multipole axis is plotted logarithmically (as in Fig. 29.1, and part of Fig. 29.2).

Time variation of the potentials (*i.e.*, time-dependent metric perturbations) at late times leads to an upturn in the C_ℓ s in the lowest several multipoles; any deviation from a total equation of state $w = 0$ has such an effect. So the dominance of the dark energy at low redshift (see Dark Energy—Sec. 28) makes the lowest ℓ s rise above the plateau. This is usually called the integrated Sachs-Wolfe effect (or ISW rise), since it comes from the line integral of $\dot{\phi}$; it has been confirmed through correlations between the large-angle anisotropies and large-scale structure [37]. Specific models can also give additional contributions at low ℓ (*e.g.*, perturbations in the dark-energy component itself [38]), but typically these are buried in the cosmic variance.

In principle, the mechanism that produces primordial perturbations could generate scalar, vector, and tensor modes. However, the vector (vorticity) modes decay with the expansion of the Universe. The tensors (transverse trace-free perturbations to the metric) generate temperature anisotropies through the integrated effect of the locally-anisotropic expansion of space. Since the tensor modes also redshift away after they enter the horizon, they contribute only to angular scales above about 1° (see Fig. 29.1). Hence, some fraction of the low- ℓ signal could be due to a gravitational wave contribution, although small amounts of tensors are essentially impossible to discriminate from other effects that might raise the level of the plateau. Nevertheless, the tensors *can* be distinguished using polarization information (see Sec. 29.7).

29.5.2 The Acoustic Peaks, $100 \lesssim \ell \lesssim 1000$

On sub-degree scales, the rich structure in the anisotropy spectrum is the consequence of gravity-driven acoustic oscillations occurring before the atoms in the Universe became neutral [39]. Perturbations inside the horizon at last scattering were able to evolve causally and produce anisotropy at the last-scattering epoch, which reflects this evolution. The frozen-in phases of these sound waves imprint a dependence on the cosmological parameters, which gives CMB anisotropies their great constraining power.

The underlying physics can be understood as follows. Before the Universe became neutral, the proton-electron plasma was tightly coupled to the photons, and these components behaved as a single ‘photon-baryon fluid.’ Perturbations in the gravitational potential, dominated by the dark-matter component, were steadily evolving. They drove oscillations in the photon-baryon fluid, with photon pressure providing most of the restoring force and baryons giving some additional inertia. The perturbations were quite small in amplitude, $\mathcal{O}(10^{-5})$, and so evolved linearly. That means each Fourier mode developed independently, and hence can be described as a driven harmonic oscillator, with frequency determined by the sound speed in the fluid. Thus, the fluid density underwent oscillations, giving time variations in temperature. These combine with a velocity effect, which is $\pi/2$ out of phase and has its amplitude reduced by the sound speed.

After the Universe recombined, the radiation decoupled from the baryons and could travel freely towards us. At that point, the (temporal) phases of the oscillations were frozen-in, and became

projected on the sky as a harmonic series of peaks and troughs in power. The main peak is the mode that went through 1/4 of a period, reaching maximal compression. The even peaks are maximal *under-densities*, which are generally of smaller amplitude because the rebound has to fight against the baryon inertia. The troughs, which do not extend to zero power, are partially filled by the Doppler effect because they are at the velocity maxima.

The physical length scale associated with the peaks is the sound horizon at last scattering, which can be straightforwardly calculated. This length is projected onto the sky, leading to an angular scale that depends on the geometry of space, as well as the distance to last scattering. Hence, the angular position of the peaks is a sensitive probe of a particular combination of cosmological parameters. In fact, this characteristic angular scale, θ_* , is the most precisely measured observable, and hence is usually treated as an element of the cosmological parameter set.

One additional effect arises from reionization at redshift z_i . A fraction of photons (τ) will be isotropically scattered at $z < z_i$, partially erasing the anisotropies at angular scales smaller than those subtended by the Hubble radius at z_i . This corresponds typically to ℓs above about 10, depending on the specific reionization model. The acoustic peaks are therefore reduced by a factor $e^{-2\tau}$ relative to the plateau.

These acoustic peaks were a clear theoretical prediction going back to about 1970 [40]. One can think of them as a snapshot of stochastic standing waves. Since the physics governing them is simple and their structure rich, one can see how they encode extractable information about the cosmological parameters. Their empirical existence started to become clear around 1994 [41], and the emergence, over the following decade, of a coherent series of acoustic peaks and troughs is a triumph of modern cosmology. This picture has received further confirmation with the detection in the power spectrum of galaxies (at redshifts $z \lesssim 1$) of the imprint of these same acoustic oscillations in the baryon component [42], as well as through detection of the expected oscillations in CMB polarization power spectra (see Sec. 29.7).

29.5.3 The Damping Tail, $\ell \gtrsim 1000$

The recombination process is not instantaneous, and this imparts a thickness to the LSS. This leads to a damping of the anisotropies at the highest ℓs , corresponding to scales smaller than that subtended by this thickness. One can also think of the photon-baryon fluid as having imperfect coupling, so that there is diffusion between the two components, and hence the amplitudes of the oscillations decrease with time. These effects lead to a damping of the $C_{\ell s}$, sometimes called ‘Silk damping’ [43], which cuts off the anisotropies at multipoles above about 2000. So, although in principle it is possible to measure to ever smaller scales, this becomes increasingly difficult in practice.

29.5.4 Gravitational Lensing Effects

CMB gravitational lensing is caused by structures at lower redshift along the line of sight to the LSS. Photon paths are deflected by the lensing potential ϕ , such that $T(\hat{n}) \rightarrow T(\hat{n} + \nabla\phi)$. Typical deflections are around 2 arcmin, but coherent over scales of a degree or so. Lensing preserves surface brightness, which means that a uniform temperature field would be unaffected; however, since there are anisotropies, then several distinct effects can be identified. The $C_{\ell s}$ are convolved with a smoothing function in a calculable way, partially flattening the peaks and troughs, generating a power-law tail at the highest multipoles, and complicating the polarization signal [44] (see Sec. 29.7.3). Additionally, the effect of lensing on the CMB can be detected through the 4-point function, which correlates temperature gradients and small-scale anisotropies, enabling a map of the lensing potential to be constructed [45].

Lensing is important because it gives an independent estimate of A_s , breaking the parameter combination $A_s e^{-2\tau}$ that is largely degenerate in the temperature anisotropy power spectra. Lens-

ing is an example of a ‘secondary effect,’ *i.e.*, the processing of anisotropies due to relatively nearby structures (see Sec. 29.9.2). Galaxies and clusters of galaxies give several such effects; all are expected to be of low amplitude, but are increasingly important at the highest ℓ s. Such effects carry additional cosmological information (about evolving gravitational potentials in the low-redshift Universe) and are receiving more attention as experiments push to higher sensitivity and angular resolution. The lensing power spectrum (see Sec. 29.8) can potentially constrain dark-energy evolution, while future measurements at high ℓ are a particularly sensitive probe of the sum of the neutrino masses [46].

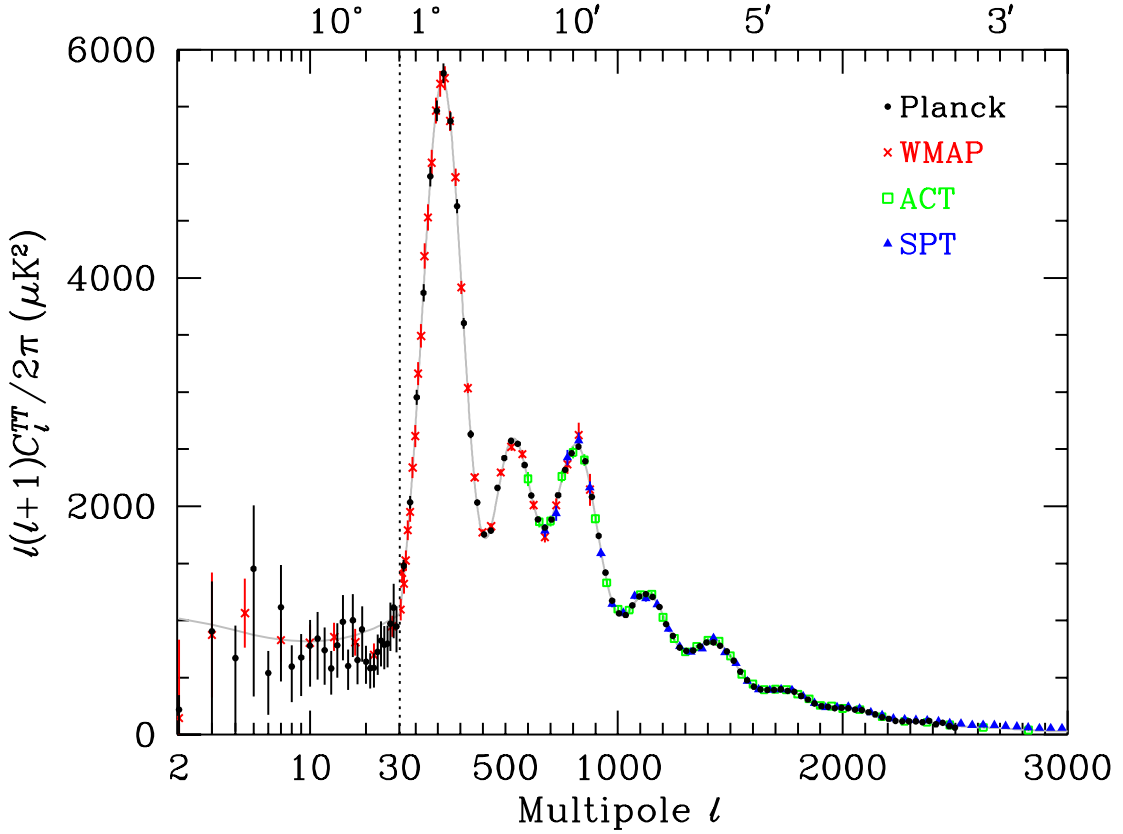


Figure 29.2: CMB temperature anisotropy band-power estimates from the *Planck*, *WMAP*, ACT, and SPT experiments. Note that the widths of the multipole bands vary between experiments and have not been plotted. This figure represents only a selection of the most recent available experimental results, and some points with large error bars have been omitted. At the higher multipoles these band-powers involve subtraction of particular foreground models, and so proper analysis requires simultaneous fitting of CMB and foregrounds over multiple frequencies. The horizontal axis here is logarithmic for the lowest multipoles, to show the Sachs-Wolfe plateau, and linear for the other multipoles. The acoustic peaks and damping region are very clearly observed, with no need for a theoretical line to guide the eye; however, the curve plotted is the best-fit *Planck* Λ CDM model.

29.6 Current Temperature Anisotropy Data

Steady improvement in CMB data quality has led to the present-day cosmological model. The most robust constraints currently available come from *Planck* satellite [47, 48] data (together with

constraints from non-CMB cosmological data sets), although smaller-scale results from the ACT [49] and SPT [50] experiments are beginning to add useful constraining power. We plot power spectrum estimates from these experiments in Fig. 29.2, along with *WMAP* data [5] for comparison (see previous versions of this review for data from earlier experiments). Independent experimental data show consistency, both in maps and in derived power spectra (up to systematic uncertainties in the overall calibration for some experiments). This makes it clear that systematic effects are largely under control.

The band-powers shown in Fig. 29.2 are in very good agreement with a ‘ Λ CDM’ model. As described earlier, several (at least seven) of the peaks and troughs are quite apparent. The original papers present the details on how these estimates were made, on the band-power correlation strengths, and on the information needed for their proper interpretation.

29.7 CMB Polarization

Thomson scattering of an anisotropic radiation field also generates linear polarization and the CMB is predicted to be polarized, at the level of roughly 5% of the temperature anisotropies [51]. Polarization is a spin-2 field on the sky, and the algebra of the modes in multipole space is strongly analogous to spin-orbit coupling in quantum mechanics [52]. The linear polarization pattern can be decomposed in a number of ways, with two quantities required for each pixel in a map, often given as the Q and U Stokes parameters. However, the most intuitive and physical decomposition is a geometrical one, splitting the polarization pattern into a part that comes from a divergence (often referred to as the ‘ E mode’) and a part with a curl (called the ‘ B mode’) [53]. More explicitly, the modes are defined in terms of second derivatives of the polarization amplitude, with the Hessian for the E modes having principal axes in the same sense as the polarization, while the B -mode pattern can be thought of as a 45° rotation of the E -mode pattern. Globally one sees that the E modes have $(-1)^\ell$ parity (like the spherical harmonics), while the B modes have $(-1)^{\ell+1}$ parity.

The existence of this linear polarization allows for six different cross-power spectra to be determined from data that measure the full temperature and polarization anisotropy information. Parity considerations make two of these zero, and we are left with four potential observables, C_ℓ^{TT} , C_ℓ^{TE} , C_ℓ^{EE} , and C_ℓ^{BB} (see Fig. 29.1). Because scalar perturbations have no handedness, the B -mode power spectrum can only be sourced by vectors or tensors. Moreover, inflationary scalar perturbations give only E modes, while tensors generate roughly equal amounts of E and B , therefore the determination of a non-zero B -mode signal is a way to measure the gravitational-wave contribution (and thus potentially derive the energy scale of inflation). However, because the signal is expected to be rather weak, one must first eliminate the foreground contributions and other systematic effects down to very low levels. In addition, CMB lensing creates B modes from E modes, further complicating the extraction of a tensor signal.

As with temperature, the polarization C_ℓ s exhibit a series of acoustic peaks generated by the oscillating photon-baryon fluid. The main ‘ EE ’ power spectrum has peaks that are out of phase with those in the ‘ TT ’ spectrum because the polarization anisotropies are sourced by the fluid velocity. The ‘ TE ’ part of the polarization and temperature patterns comes from correlations between density and velocity perturbations on the last-scattering surface, which can be both positive and negative, and is of larger amplitude than the EE signal. There is no polarization Sachs-Wolfe effect, and hence no large-angle (low- ℓ) plateau. However, scattering during a recent period of reionization can create a polarization ‘bump’ at large angular scales.

Because the polarization anisotropies have only a small fraction of the amplitude of the temperature anisotropies, they took longer to detect. The first measurement of a polarization signal came in 2002 from the DASI experiment [54], which provided a convincing detection, confirming the general paradigm, but of low enough significance that it lent no real constraint to models.

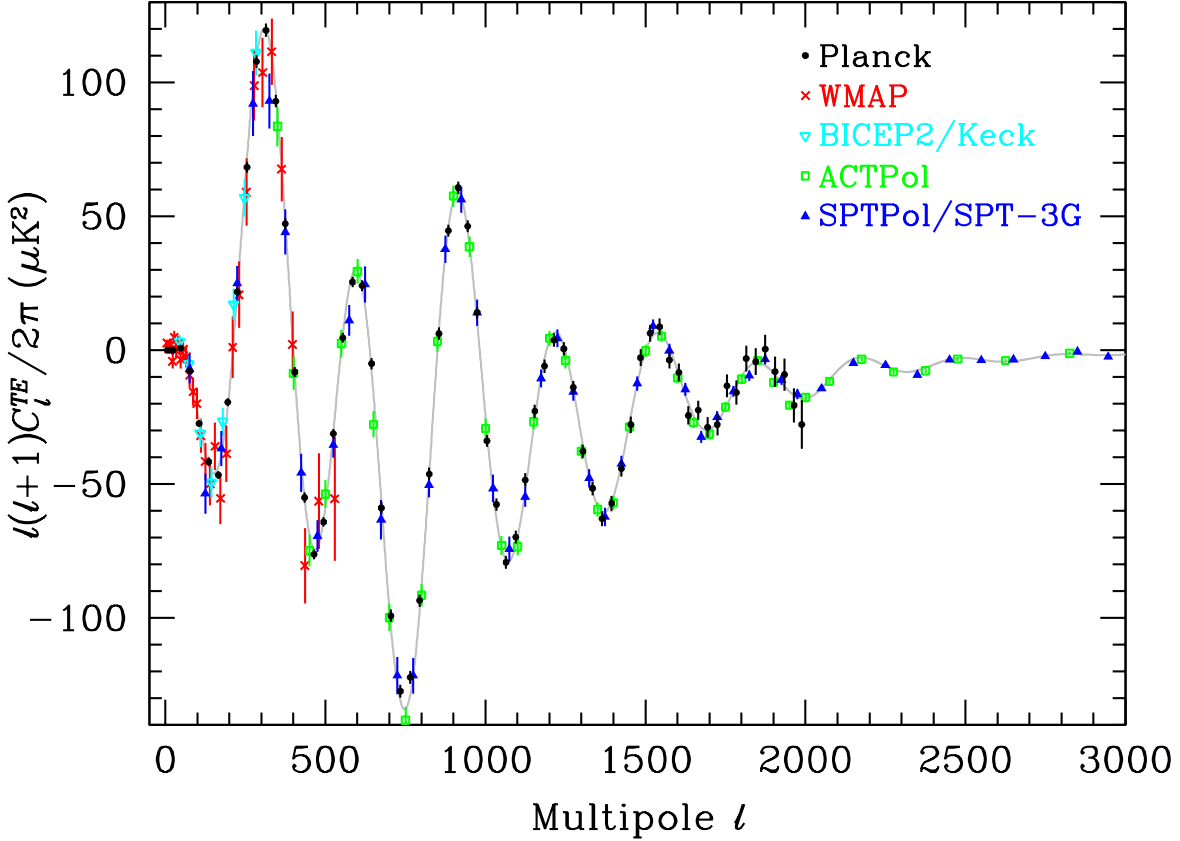


Figure 29.3: Cross-power spectrum band-powers of the temperature anisotropies and E -mode polarization signal from *Planck* (the low multipole data have been binned here), as well as *WMAP*, BICEP2/Keck, ACTPol, and SPTPol/SPT-3G. The curve is the best fit to the *Planck* temperature, polarization, and lensing band-powers. Note that each data point is an average over a band of multipoles, and hence to compare in detail with a model one has to integrate the theoretical curve through the band.

Despite dramatic progress since then, it is still the case that polarization data mainly support the basic paradigm, while reducing error bars on parameters by only around 20%. However, there are exceptions to this, specifically in the reionization optical depth, and the potential to constrain primordial gravitational waves. Moreover, the situation is expected to change dramatically as more of the available polarization modes are measured.

29.7.1 T - E Power Spectrum

Because the T and E skies are correlated, one has to measure the TE power spectrum, as well as TT and EE , in order to extract all the cosmological information. This TE signal has now been mapped out extremely accurately by *Planck* [48], and these band-powers are shown in Fig. 29.3, along with those from *WMAP* [55] and BICEP2/Keck [56], with ACTPol [57] and SPTPol/-SPT-3G [58, 59] extending to smaller angular scales. The anti-correlation at $\ell \simeq 150$ and the peak at $\ell \simeq 300$ were the first features to become distinct, but now a whole series of oscillations is clearly seen in this power spectrum (including six or seven peaks and troughs [10]). The measured shape of the

cross-correlation power spectrum provides supporting evidence for the general cosmological picture, and also directly constrains the thickness of the last-scattering surface. Because the polarization anisotropies are generated in this scattering surface, the existence of correlations at angles above about a degree demonstrates that there were super-Hubble fluctuations at the recombination epoch. The sign of this correlation also confirms the adiabatic paradigm.

The overall picture of the source of CMB polarization and its oscillations has also been confirmed through tests that average the maps around both temperature hot spots and cold spots [60]. One sees precisely the expected patterns of radial and tangential polarization configurations, as well as the phase shift between polarization and temperature. This leaves no doubt that the oscillation picture is the correct one and that the polarization is coming from Thomson scattering at $z \simeq 1100$.

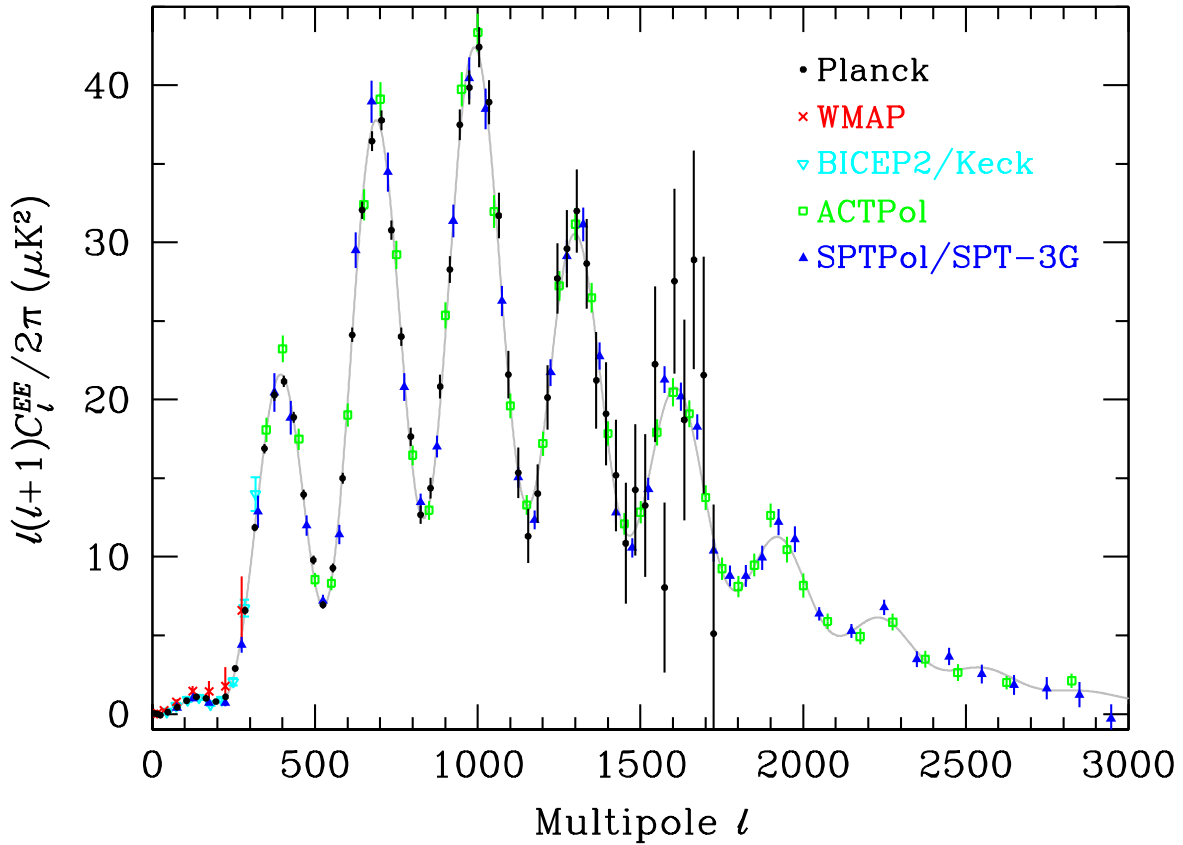


Figure 29.4: Power spectrum of E -mode polarization from *Planck*, together with *WMAP*, BICEP2/Keck Array [56], ACTPol [57], and SPTPol/SPT-3G [58, 59] are shown in Fig. 29.4. Without the benefit of correlating with the temperature anisotropies (*i.e.*, measuring C_ℓ^{TE}), the polarization anisotropies are very weak and challenging to measure. Nevertheless, the oscillatory pattern is now well established and the data

29.7.2 E - E Power Spectrum

Experimental band-powers for C_ℓ^{EE} from *Planck*, *WMAP*, BICEP2/Keck Array [56], ACTPol [57], and SPTPol/SPT-3G [58, 59] are shown in Fig. 29.4. Without the benefit of correlating with the temperature anisotropies (*i.e.*, measuring C_ℓ^{TE}), the polarization anisotropies are very weak and challenging to measure. Nevertheless, the oscillatory pattern is now well established and the data

closely match the TT -derived theoretical prediction. In Fig. 29.4 one can clearly see the ‘shoulder’ expected at $\ell \simeq 140$, the first main peak at $\ell \simeq 400$ (corresponding to the first trough in C_ℓ^{TT}), and the series of oscillations that is out of phase with those of the temperature anisotropy power spectrum (including six or seven peaks and troughs [10]).

Perhaps the most unique result from the polarization measurements is at the largest angular scales ($\ell < 10$) in C_ℓ^{TE} and C_ℓ^{EE} , where there is evidence for an excess signal (not visible in Fig. 29.4) compared to that expected from the temperature power spectrum alone. This is precisely the signal anticipated from an early period of reionization, arising from Doppler shifts during the partial scattering at $z < z_i$. The amplitude of the signal indicates that the first stars, presumably the source of the ionizing radiation, formed around $z \simeq 8$ (although the uncertainty is still quite large). This corresponds to a scattering optical depth $\tau \simeq 0.06$, so roughly 6% of CMB photons were re-scattered at the reionization epoch, with the other 94% last scattering at $z \simeq 1100$. However, estimates of the amplitude of this reionization excess have come down since the first measurements by *WMAP* (indicating that this is an extremely difficult measurement to make) and the latest *Planck* results have reduced the value further [11, 61].

29.7.3 B - B Power Spectrum

The expected amplitude of C_ℓ^{BB} is very small, so measurements of this polarization curl-mode are extremely challenging. The first indication of the existence of the BB signal came from the detection of the expected conversion of E modes to B modes by gravitational lensing, through a correlation technique using the lensing potential and polarization measurements from SPT [62]. However, the real promise of B modes lies in the detection of primordial gravitational waves at larger scales. This tensor signature could be seen either in the ‘recombination bump’ at around $\ell = 100$ (caused by an ISW effect as gravitational waves redshift away at the last-scattering epoch) or the ‘reionization bump’ at $\ell \lesssim 10$ (from additional scattering at low redshifts).

Results from the BICEP2 experiment [63] in 2014 suggested a detection of the primordial B -mode signature around the recombination peak. BICEP2 mapped a small part of the CMB sky with the best sensitivity level reached at that time (below 100 nK), but at a single frequency. Higher frequency data from *Planck* indicated that much of the BICEP2 signal was due to dust within our Galaxy, and a combined analysis by the BICEP2, Keck Array, and *Planck* teams [64] indicated that the data are consistent with no primordial B modes. The current constraint from *Planck* data alone is $r < 0.069$ (95% at $k = 0.05 \text{ Mpc}^{-1}$ [11, 61]) using all CMB power spectra, and this limit is reduced to $r < 0.044$ with the inclusion of BICEP2/Keck Array data [61, 65]. The most constraining limit is $r < 0.036$ from a combination of BICEP2, Keck Array, and BICEP3 data, using *WMAP* and *Planck* maps to help remove foregrounds [66].

Several experiments are continuing to push down the sensitivity of B -mode measurements, motivated by the enormous importance of a future detection of this telltale signature of inflation (or other physics at the highest energies). A compilation of experimental results for C_ℓ^{BB} is shown in Fig. 29.5, coming from a combination of direct estimates of the B modes (BICEP2/BICEP3/Keck Array [66], POLARBEAR [67], SPTPol [68], and ACTPol [57]) and indirect determinations of the lensing B modes based on estimating the effect of measured lensing on measured E modes (*Planck* [69], SPT [62], and ACT [70]). Additional band-power estimates are expected from these and other experiments in the near future, with the Simons Observatory [71], the so-called ‘Stage 4’ CMB project [72] and the *LiteBIRD* satellite [73], holding great promise for pushing down to the $r \sim 0.001$ level.

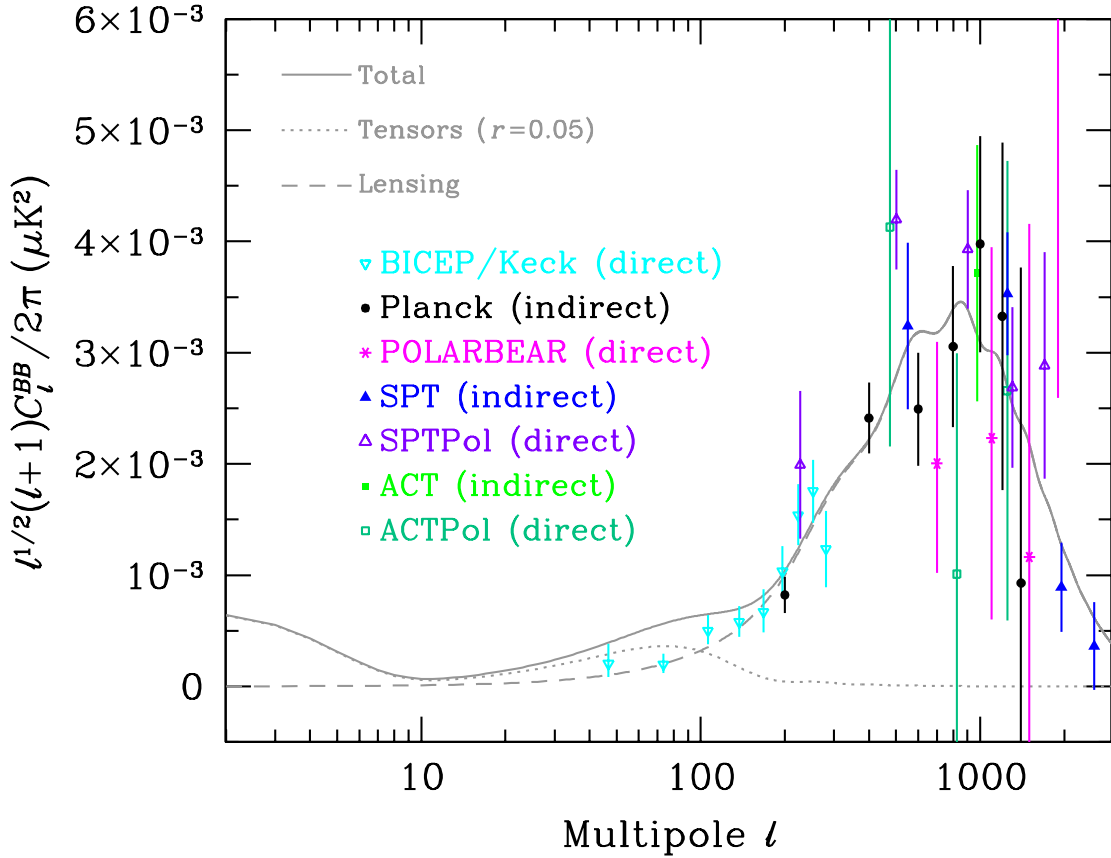


Figure 29.5: Power spectrum of B -mode polarization, including results from the BICEP2/BICEP3/Keck Array combined analysis, *Planck*, POLARBEAR, SPT, and ACT. Note that some of the measurements are direct estimates of B modes on the sky, while others are only sensitive to the lensing signal and come from combining E -mode and lensing potential measurements. Several earlier experiments reported upper limits, which are all off the top of this plot. A logarithmic horizontal axis is adopted here and the y -axis has been divided by a factor of $\sqrt{\ell}$ in order to show all three theoretically expected contributions: the low- ℓ reionization bump; the $\ell \simeq 100$ recombination peak; and the high- ℓ lensing signature. The dotted line is for a tensor (primordial gravitational wave) fraction $r = 0.05$, simply as an example, with all other cosmological parameters set at the best *Planck*-derived values, for which model the expected lensing B modes have also been shown with a dashed line.

29.8 CMB Lensing Power Spectrum

One further CMB observable is the gravitational lensing deflection, leading to the construction of a map of the lensing potential. The latest *Planck* results [74] give a map that is detected at the $> 40\sigma$ level using a minimum-variance procedure from the 4-point function of temperature and polarization data. From these maps, estimates can be constructed of $C_\ell^{\phi\phi}$, the lensing-potential power spectrum, which is found to be consistent with predictions from the best-fit temperature and polarization model. Recent results from ACT give a power spectrum that has a similar overall signal-to-noise ratio [75] and there are also interesting measurements from SPT [76]. Figure 29.6 plots the *Planck*, ACT, and SPT estimates of $C_\ell^{\kappa\kappa}$, the lensing convergence power spectrum, which

is proportional to $\ell^2(\ell+1)^2$ times the potential power spectrum $C_\ell^{\phi\phi}$.

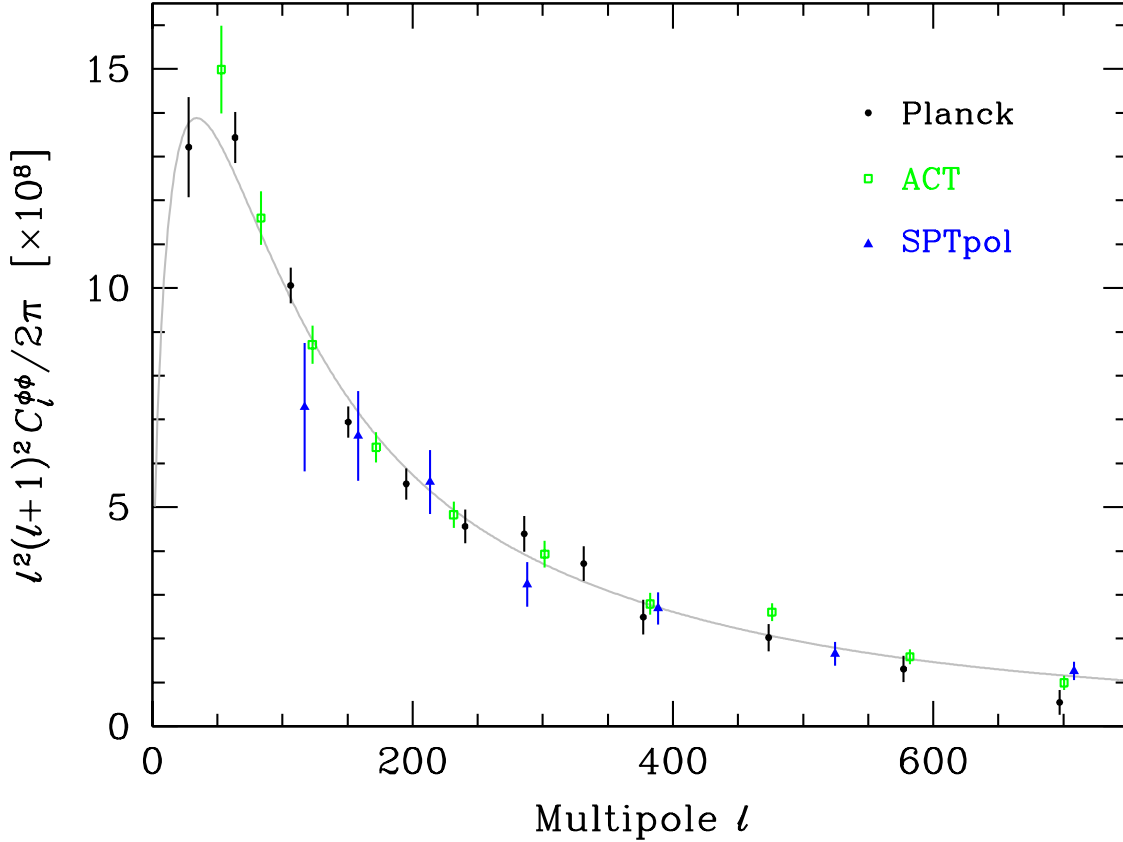


Figure 29.6: Power spectrum measurements for CMB lensing, including selected results from *Planck*, ACT, and SPT. The quantity plotted is the (dimensionless) potential power spectrum, scaled by $\ell^2(\ell+1)^2$ and multiplied by a factor of 10^8 to make the numbers more manageable. Some less reliable measurements have not been plotted. The best-fit *Planck* Λ CDM spectrum is plotted as a gray line.

We can think of each sky pixel as possessing three independent quantities that can be measured, namely T , E , and ϕ (and potentially B , if that becomes detectable). Determining the constraining power comes down to counting $Y_{\ell m}$ modes [77], as well as appreciating that some modes help to break particular parameter degeneracies. We have only scratched the surface of CMB lensing so far, and it is expected that future small-scale experiments will be able to extract more of the cosmological information. Further constraints can also be derived on the lower-redshift Universe by cross-correlating CMB lensing with other cosmological tracers of large-scale structure. Additionally, small-scale lensing, combined with E -mode measurements, can be used to ‘delens’ CMB B -mode data, which will be important for pushing down into the $r \lesssim 0.01$ regime [78].

29.9 Complications

There are a number of issues that complicate the interpretation of CMB anisotropy data (and are considered to be *signal* by many astrophysicists), some of which we sketch out below.

29.9.1 Foregrounds

The microwave sky contains significant emission from our Galaxy and from extragalactic sources [79]. Fortunately, the frequency dependence of these various sources is in general substantially different from that of the CMB anisotropy signals. The combination of Galactic synchrotron, bremsstrahlung, and dust emission reaches a minimum at a frequency of roughly 100 GHz (or wavelength of about 3 mm). As one moves to greater angular resolution, the minimum moves to slightly higher frequencies, but becomes more sensitive to unresolved (point-like) sources.

At frequencies around 100 GHz, and for portions of the sky away from the Galactic plane, the foregrounds are typically 1 to 10% of the CMB anisotropies. By making observations at multiple frequencies, it is relatively straightforward to separate the various components and determine the CMB signal to the few per cent level. For greater sensitivity, it is necessary to use the spatial information and statistical properties of the foregrounds to separate them from the CMB. Furthermore, at higher ℓ s it is essential to carefully model extragalactic foregrounds, particularly the clustering of infrared-emitting galaxies and scattering due to galaxy clusters, which dominate the measured power spectrum as we move into the damping tail.

The foregrounds for CMB polarization follow a similar pattern to those for temperature, but are intrinsically brighter relative to CMB anisotropies. *WMAP* showed that the polarized foregrounds dominate at large angular scales, and that they must be well characterized in order to be discriminated [80]. *Planck* has shown that it is possible to characterize the foreground polarization signals, with synchrotron dominating at low frequencies and dust at high frequencies [81]. On smaller scales there are no strongly-polarized foregrounds, and hence at high multipoles it is in principle easier to measure foreground-free modes in polarization than in temperature. Although foreground contamination will no doubt become more complicated as we push down in sensitivity, making analysis more difficult, for the time being, foreground contamination is not a fundamental limit for CMB experiments.

29.9.2 Secondary Anisotropies

With increasingly precise measurements of the primary anisotropies, there is growing theoretical and observational interest in ‘secondary anisotropies,’ pushing experiments to higher angular resolution and sensitivity. These secondary effects arise from the processing of the CMB due to ionization history and the evolution of structure, including gravitational lensing (which was already discussed) and patchy reionization effects [82]. Additional information can thus be extracted about the Universe at $z \ll 1000$. This tends to be most effectively done through correlating CMB maps with other cosmological probes of structure. Secondary signals are also typically non-Gaussian, unlike the primary CMB anisotropies.

A secondary signal of great current interest is the Sunyaev-Zeldovich (SZ) effect [83], which is Compton scattering ($\gamma e \rightarrow \gamma' e'$) of the CMB photons by hot electrons in intergalactic plasma. This creates spectral distortions by transferring energy from the electrons to the photons. It is particularly important for clusters of galaxies, through which one observes a partially Comptonized spectrum, resulting in a decrement at radio wavelengths and an increment in the submillimeter.

The imprint on the CMB sky is of the form $\Delta T/T = y f(x)$, with the y parameter being the integral of Thomson optical depth times kT_e/m_ec^2 through the cluster, and $f(x)$ describing the frequency dependence. This is simply $x \coth(x/2) - 4$ for a non-relativistic gas (the electron temperature in a cluster is typically a few keV), where the dimensionless frequency $x \equiv h\nu/kT_\gamma$. As well as this ‘thermal’ SZ effect, there is also a smaller ‘kinetic’ effect due to the bulk motion of the cluster gas, giving $\Delta T/T \sim \tau(v/c)$, with either sign, but having the same spectrum as the primary CMB anisotropies.

A significant advantage in finding galaxy clusters via the SZ effect is that the signal is largely

independent of redshift, so in principle clusters can be found to arbitrarily large distances. The SZ effect can be used to find and study individual clusters, and to obtain estimates of the Hubble constant. There is also the potential to constrain other cosmological parameters, such as the clustering amplitude σ_8 and the equation of state of the dark energy, through counts of detected clusters as a function of redshift. The promise of the method has been realized through detections of clusters purely through the SZ effect by SPT [84], ACT [85], and *Planck* [86]. Results from *Planck* clusters [87] suggest a somewhat lower value of σ_8 than inferred from CMB anisotropies, but there are still systematic uncertainties that might encompass the difference, and a more recent analysis of SPT-detected clusters shows better agreement [88]. Further analysis of scaling relations among cluster properties should enable more robust cosmological constraints to be placed in future, so that we can understand whether this ‘tension’ might be a sign of new physics.

29.9.3 Higher-order Statistics

Although most of the CMB anisotropy information is contained in the power spectra, there will also be weak signals present in higher-order statistics. These can measure any primordial non-Gaussianity in the perturbations, as well as non-linear growth of the fluctuations on small scales and other secondary effects (plus residual foreground contamination of course). There are an infinite variety of ways in which the CMB could be non-Gaussian [26]; however, there is a generic form to consider for the initial conditions, where a quadratic contribution to the curvature perturbations is parameterized through a dimensionless number f_{NL} . This weakly non-linear component can be constrained in several ways, the most popular being through measurements of the bispectrum (or 3-point function).

The constraints depend on the shape of the triangles in harmonic space, and it has become common to distinguish the ‘local’ or ‘squeezed’ configuration (in which one side is much smaller than the other two) from the ‘equilateral’ configuration. Other configurations are also relevant for specific theories, such as ‘orthogonal’ non-Gaussianity, which has positive correlations for $k_1 \simeq 2k_2 \simeq 2k_3$, and negative correlations for the equilateral configuration. The constraints from the *Planck* team [89] are $f_{\text{NL}}^{\text{local}} = 1 \pm 5$, $f_{\text{NL}}^{\text{equil}} = -26 \pm 47$, and $f_{\text{NL}}^{\text{ortho}} = -38 \pm 24$.

These results are consistent with zero, but are at a level that is now interesting for model predictions. The amplitude of f_{NL} expected is small, so that a detection of $f_{\text{NL}} \gg 1$ would rule out all single-field, slow-roll inflationary models. It is still possible to improve upon these *Planck* results, and it certainly seems feasible that a measurement of primordial non-Gaussianity may yet be within reach. *Non*-primordial detections of non-Gaussianity from expected signatures have already been made. For example, the bispectrum and trispectrum contain evidence of gravitational lensing, the ISW effect, and Doppler boosting. For now the primordial signal is elusive, but should it be detected, then detailed measurements of non-Gaussianity will become a unique probe of inflationary-era physics. Because of that, much effort continues to be devoted to honing predictions and measurement techniques, with the expectation that we will need to go beyond the CMB (*e.g.*, 3D galaxy surveys) to dramatically improve the constraints.

29.9.4 Anomalies

Several features seen in the *Planck* data [29, 60, 90] confirm those found earlier with *WMAP* [28], showing mild deviations from a simple description of the sky; these are often referred to as ‘anomalies.’ One such feature is the lack of power in the multipole range $\ell \simeq 20\text{--}30$ [11, 48]. Other examples involve the apparent breaking of statistical anisotropy, caused by alignment of the lowest multipoles, as well as a somewhat excessive cold spot and a power asymmetry between hemispheres. No such feature is significant at more than the roughly 3σ level, and the importance of ‘*a posteriori*’ statistics here has been emphasized by many authors. Since these effects are at large angular scales, where cosmic variance dominates, the results will not increase in significance

with more data, although there is the potential for more sensitive polarization measurements to provide independent tests.

29.10 Constraints on Cosmological Parameters

The most striking outcome of the last couple of decades of experimental results is that the standard cosmological paradigm continues to be in very good shape. A large amount of high-precision data on the CMB power spectrum is adequately fit with fewer than 10 free parameters (and only six need non-trivial values). The framework is that of FRW models, which have nearly flat geometry, containing dark matter and dark energy, and with adiabatic perturbations having close to scale-invariant initial conditions.

Within this basic picture, the values of the cosmological parameters can be constrained. Of course, more stringent bounds can be placed on models that cover a restricted parameter space, *e.g.*, assuming that $\Omega_{\text{tot}} = 1$ or $r = 0$. More generally, the constraints depend upon the adopted prior probability distributions, even if they are implicit, for example by restricting the parameter freedom or their ranges (particularly where likelihoods peak near the boundaries), or by using different choices of other data in combination with the CMB. As the data become even more precise, these considerations will be less important, but for now we caution that restrictions on model space and choice of non-CMB data sets and priors need to be kept in mind when adopting specific parameter values and uncertainties.

There are some combinations of parameters that fit the CMB anisotropies almost equivalently. For example, there is a nearly exact geometric degeneracy, where any combination of Ω_m and Ω_Λ that provides the same angular-diameter distance to last scattering will give nearly identical C_ℓ s. There are also other less exact degeneracies among the parameters. Such degeneracies can be broken when using the CMB results in combination with other cosmological data sets. Particularly useful are complementary constraints from baryon acoustic oscillations, galaxy clustering, the abundance of galaxy clusters, weak gravitational lensing measurements, and Type Ia supernova distances. For an overview of some of these other cosmological constraints, see The Cosmological Parameters—Sec. 25 of this *Review*.

Within the context of a 6-parameter family of models (which fixes $\Omega_{\text{tot}} = 1$, $dn_s/d\ln k = 0$, $r = 0$, and $w = -1$) the *Planck* results for *TT*, together with *TE*, *EE*, and CMB lensing, yield [11]: $\ln(10^{10}A_s) = 3.044 \pm 0.014$; $n_s = 0.965 \pm 0.004$; $\Omega_b h^2 = 0.02237 \pm 0.00015$; $\Omega_c h^2 = 0.1200 \pm 0.0012$; $100\theta_* = 1.04092 \pm 0.00031$; and $\tau = 0.054 \pm 0.007$. Other parameters can be derived from this basic set, including $h = 0.674 \pm 0.005$, $\Omega_\Lambda = 0.685 \pm 0.007$ ($= 1 - \Omega_m$) and $\sigma_8 = 0.811 \pm 0.006$ (see also Astrophysical Constants and Parameters—Sec. 2). Somewhat different (although consistent) values are obtained using other data combinations, such as including BAO, supernova, H_0 , or weak-lensing constraints (see Sec. 25 of this *Review*). However, the *Planck* results quoted above are currently the best available from CMB data alone. Results from other CMB experiments (*e.g.*, SPT-3G [59]) are consistent and becoming competitive.

The standard cosmological model still fits the data well, with the error bars on the parameters continuing to shrink. Improved measurement of higher acoustic peaks has dramatically reduced the uncertainty in the θ_* parameter, which is now detected at $> 3000\sigma$. The evidence for $n_s < 1$ is now at the 8σ level from *Planck* data alone. The value of the reionization optical depth has decreased compared with earlier estimates; it is convincingly detected, but still not at very high significance.

The inferred value of H_0 is smaller than the most precise values derived from the cosmic distance ladder. This parameter tension is discussed more fully in other sections of this *Review*. The CMB anisotropies also provide the most precise estimate of the age of the Universe, with *Planck* giving the value $t_0 = 13.797 \pm 0.023$ Gyr.

Constraints can also be placed on parameters beyond the basic six, particularly when including

other astrophysical data sets. Relaxing the flatness assumption, the constraint on Ω_{tot} is 1.011 ± 0.006 . Note that for h , the CMB data alone provide only a very weak constraint if spatial flatness is not assumed. However, with the addition of other data (particularly powerful in this context being a compilation of BAO measurements; see Sec. 25 of this *Review*), the constraints on the Hubble constant and curvature improve considerably, leading to $\Omega_{\text{tot}} = 0.9993 \pm 0.0019$ [11].

For $\Omega_b h^2$ the CMB-derived value is generally consistent with completely independent constraints from Big Bang nucleosynthesis (see Sec. 24 of this *Review*). Related are constraints on additional neutrino-like relativistic degrees of freedom, which lead to $N_{\text{eff}} = 2.99 \pm 0.17$ (including BAO), *i.e.*, no evidence for extra neutrino species.

The tightest published limit on the tensor-to-scalar ratio is $r < 0.036$ (measured at $k = 0.05 \text{ Mpc}^{-1}$) from BICEP/Keck Array [66]. The detailed limit depends on how other parameters, especially A_s , n_t , and $dn_s/d\ln k \neq 0$ are restricted. The joint constraints on n_s and r allow specific inflationary models to be tested [30, 91]. Looking at the (n_s, r) plane, this means that $m^2\phi^2$ (mass-term quadratic) inflation is disfavored by the data, as well as $\lambda\phi^4$ (self-coupled) inflation.

The addition of the dark-energy equation of state w adds the partial degeneracy of being able to fit a ridge in (w, h) space, extending to low values of both parameters. This degeneracy is broken when the CMB is used in combination with other data sets, *e.g.*, adding a compilation of BAO and supernova data gives $w = -1.028 \pm 0.031$ [11]. Constraints can also be placed on more general dark energy and modified-gravity models [92]. However, when extending the search space, one needs to be careful not to over-interpret some tensions between data sets as evidence for new physics.

For the reionization optical depth, a reanalysis of *Planck* data in 2016 resulted in a reduction in the value of τ , with the tightest result giving $\tau = 0.055 \pm 0.009$, and the newest analyses giving similar numbers. This corresponds to $z_i = 7.8\text{--}8.8$ (depending on the functional form of the reionization history), with an uncertainty of ± 0.9 [93]. This redshift is only slightly higher than that suggested from studies of absorption lines in high- z quasar spectra [94] and Ly α -emitting galaxies [95], perhaps hinting that the process of reionization was not as complex as previously suspected. The important constraint provided by CMB polarization, in combination with astrophysical measurements, thus allows us to investigate how the first stars formed and brought about the end of the cosmic dark ages.

29.11 Particle Physics Constraints

CMB data place limits on parameters that are directly relevant for particle physics models. For example, there is a limit on the sum of the masses of the neutrinos, $\Sigma m_\nu < 0.12 \text{ eV}$ (95%) [11] coming from *Planck* together with BAO measurements (although limits are weaker when considering both N_{eff} and Σm_ν as free parameters). This assumes the usual number density of fermions, which decoupled when they were relativistic. The limit is tantalizingly only a factor of a few higher than the minimum value coming from neutrino mixing experiments (see Neutrino Mixings—Secs. 14 and 26). As well as being an indirect probe of the neutrino background, *Planck* data also require that the neutrino fluid has perturbations, *i.e.*, that it possesses a sound speed $c_s^2 \simeq 1/3$, as expected [9].

The current suite of data suggests that $n_s < 1$, with a best-fitting value about 0.035 below unity. This is already quite constraining for inflationary models, particularly along with r limits. There is no current evidence for running of the spectral index, with $dn_s/d\ln k = -0.004 \pm 0.007$ from *Planck* alone [11] (with a similar value when BAO data are included), although this is less of a constraint on models. Similarly, primordial non-Gaussianity is being probed to interesting levels, although tests of simple inflationary models will only come with significant reductions in uncertainty.

The large-angle anomalies, such as the hemispheric modulation of power and the dip in power at $\ell \simeq 20\text{--}30$, have the potential to be hints of new physics. Such effects might be expected in a Universe that has a large-scale power cut-off, or anisotropy in the initial power spectrum, or is

topologically non-trivial. However, cosmic variance and *a posteriori* statistics limit the significance of these anomalies, absent the existence of a model that naturally yields some of these features (and ideally also predicting other phenomena that can be tested).

Constraints on ‘cosmic birefringence’ (*i.e.*, rotation of the plane of CMB polarization that generates non-zero TB and EB power) can be used to place limits on theories involving parity violation, Lorentz violation, or axion-photon mixing [96].

It is possible to place limits on additional areas of physics [97], for example annihilating dark matter [9, 9], primordial magnetic fields [98], and time variation of the fine-structure constant [99], as well as the neutrino chemical potential, a contribution of warm dark matter, topological defects, or physics beyond general relativity. Further particle physics constraints will follow as the smaller-scale and polarization measurements continue to improve.

The CMB anisotropy measurements precisely pin down physics at the time of last-scattering, and so any change of physics can be constrained if it affects the relevant energies or timescales. Future, higher sensitivity measurements of the CMB frequency spectrum will push the constraints back to cover energy injection at much earlier times (~ 1 year). Comparison of CMB and BBN observables extend these constraints to timescales of order seconds, and energies in the MeV range. And to the extent that inflation provides an effective description of the generation of perturbations, the inflationary observables may constrain physics at GUT-type energy scales.

More generally, careful measurement of the CMB power spectra and non-Gaussianity can in principle put constraints on physics at the highest energies, including ideas of quantum gravity, string theory, extra dimensions, colliding branes, *etc.* At the moment any calculation of predictions appears to be far from definitive. However, there is a great deal of activity on implications of fundamental theories for the early Universe, and hence a chance that there might be observational implications for specific scenarios.

29.12 Fundamental Lessons

More important than the precise values of parameters is what we have learned about the general features that describe our observable Universe. Beyond the basic hot Big Bang picture, the CMB has taught us that:

- the (observable) Universe is very close to isotropic;
- the Universe recombined at $z \sim 1000$ and started to become ionized again at $z \sim 10$;
- the geometry of the Universe is close to flat;
- both dark matter and dark energy are required;
- gravitational instability is sufficient to grow all of the observed large structures in the Universe;
- topological defects were not important for structure formation;
- there were ‘synchronized’ super-Hubble modes generated in the early Universe;
- the initial perturbations were predominantly adiabatic in nature;
- the primordial perturbation spectrum has a slightly red tilt;
- the perturbations had close to Gaussian (*i.e.*, maximally random) initial conditions.

These features form the basis of the cosmological standard model, Λ CDM, for which it is tempting to make an analogy with the Standard Model of particle physics (see earlier Sections of this *Review*). In comparison, the cosmological model is much further from any underlying ‘fundamental theory,’ which might ultimately provide the values of the parameters from first principles. Nevertheless, any genuinely complete ‘theory of everything’ must include an explanation for the values of these cosmological parameters in addition to the parameters of the Standard Model of particle physics.

29.13 Future Directions

Given the significant progress in measuring the CMB sky, which has been instrumental in tying down the cosmological model, what can we anticipate for the future? There will be a steady improvement in the precision and confidence with which we can determine the appropriate cosmological parameters. Ground-based experiments operating at smaller angular scales will continue to place tighter constraints on the damping tail, lensing, and cross-correlations. New polarization experiments at small scales will probe further into the damping tail, without the limitation of extragalactic foregrounds. And polarization experiments at large angular scales will push down the limits on primordial B modes.

Planck, the third generation CMB satellite mission, was launched in May 2009, and produced a large number of papers, including a set of cosmological studies based on the first two full surveys of the sky (accompanied by a public release of data products) in 2013, a further series coming from analysis of the full mission data release in 2015 (eight surveys for the Low Frequency Instrument and five surveys for the High Frequency Instrument), and a third series derived from a final analysis of the 2018 data release, including full constraints from polarization data. *Planck* data currently dominate constraints on models, but that situation will change soon.

A set of cosmological parameters is now known to percent-level accuracy, and that may seem sufficient for many people. However, we should certainly demand more of measurements that describe *the entire observable Universe!* Hence a lot of activity in the coming years will continue to focus on determining those parameters with increasing precision. This necessarily includes testing for consistency among different predictions of the cosmological Standard Model, and searching for signals that might require additional physics.

A second area of focus will be the smaller-scale anisotropies and ‘secondary effects.’ There is a great deal of information about structure formation at $z \ll 1000$ encoded in the CMB sky. This may involve higher-order statistics and cross-correlations with other large-scale structure tracers, as well as spectral signatures, with many experiments targeting the galaxy cluster SZ effect, for example. The current status of CMB lensing is similar (in terms of total signal-to-noise) to the quality of the first CMB anisotropy measurements by *COBE*, and thus we can expect that experimental probes of lensing will improve dramatically in the coming years. All of these investigations can provide constraints on the dark-energy equation of state, for example, which is a major area of focus for several future cosmological surveys at optical wavelengths. CMB lensing also promises to yield a measurement of the sum of the neutrino masses.

A third direction is increasingly sensitive searches for specific signatures of physics at the highest energies. The most promising of these may be the primordial gravitational wave signals in C_ℓ^{BB} , which could be a probe of the $\sim 10^{16}$ GeV energy range. There are several experiments underway or being developed that are designed to search for the polarization B modes, with the most ambitious being CMB-S4 on the ground and *LiteBIRD* in space. Additionally, non-Gaussianity holds the promise of constraining models beyond single-field slow-roll inflation.

Anisotropies in the CMB have proven to be the premier probe of cosmology and the early Universe. Theoretically the CMB involves well-understood physics in the linear regime, and is under very good calculational control. A substantial and improving set of observational data now exists. Systematics appear to be under control and are not currently a limiting factor. And so for the next several years we can expect an increasing amount of cosmological information to be gleaned from CMB anisotropies, with the prospect also of some genuine surprises.

References

- [1] A. A. Penzias and R. W. Wilson, *Astrophys. J.* **142**, 419 (1965); R. H. Dicke *et al.*, *Astrophys. J.* **142**, 414 (1965).

- [2] M. White, D. Scott and J. Silk, *Ann. Rev. Astron. Astrophys.* **32**, 319 (1994); W. Hu and S. Dodelson, *Ann. Rev. Astron. Astrophys.* **40**, 171 (2002), [[arXiv:astro-ph/0110414](#)]; A. Challinor and H. Peiris, in M. Novello and S. Perez, editors, “American Institute of Physics Conference Series,” volume 1132, 86–140 (2009), [[arXiv:0903.5158](#)].
- [3] G. F. Smoot *et al.*, *Astrophys. J. Lett.* **396**, L1 (1992).
- [4] C. L. Bennett *et al.*, *Astrophys. J. Supp.* **148**, 1 (2003), [[arXiv:astro-ph/0302207](#)].
- [5] G. Hinshaw *et al.*, *Astrophys. J. Supp.* **208**, 19 (2013), [[arXiv:1212.5226](#)].
- [6] Planck Collab. 2013 Results XVI, *Astron. Astrophys.* **571**, A16 (2014), [[arXiv:1303.5076](#)].
- [7] J. A. Tauber *et al.*, *Astron. Astrophys.* **520**, A1 (2010); Planck Collab. 2013 Results I, *Astron. Astrophys.* **571**, A1 (2014), [[arXiv:1303.5062](#)].
- [8] Planck Collab. 2015 Results I, *Astron. Astrophys.* **594**, A1 (2016), [[arXiv:1502.01582](#)].
- [9] Planck Collab. 2015 Results XIII, *Astron. Astrophys.* **594**, A13 (2016), [[arXiv:1502.01589](#)].
- [10] Planck Collab. 2018 Results I, *Astron. Astrophys.* **641**, A1 (2020), [[arXiv:1807.06205](#)].
- [11] Planck Collab. 2018 Results VI, *Astron. Astrophys.* **641**, A6 (2020), [[arXiv:1807.06209](#)].
- [12] D. S. Swetz *et al.*, *Astrophys. J. Supp.* **194**, 41 (2011), [[arXiv:1007.0290](#)].
- [13] J. E. Carlstrom *et al.*, *Proc. Astron. Soc. Pacific* **123**, 568 (2011), [[arXiv:0907.4445](#)].
- [14] V. V. Klimenko *et al.*, *Astronomy Letters* **46**, 11, 715 (2020), [[arXiv:2106.00119](#)]; D. A. Riechers *et al.*, *Nature* **602**, 7895, 58 (2022), [[arXiv:2202.00693](#)].
- [15] D. J. Fixsen *et al.*, *Astrophys. J.* **734**, 5 (2011), [[arXiv:0901.0555](#)].
- [16] J. Singal *et al.*, *Proc. Astron. Soc. Pacific* **130**, 985, 036001 (2018), [[arXiv:1711.09979](#)].
- [17] A. Kogut *et al.*, *J. Cosmology Astropart. Phys.* **2011**, 7, 025 (2011), [[arXiv:1105.2044](#)]; P. André *et al.*, *J. Cosmology Astropart. Phys.* **2014**, 2, 006 (2014), [[arXiv:1310.1554](#)]; J. Delabrouille *et al.*, *Experimental Astronomy* **51**, 3, 1471 (2021), [[arXiv:1909.01591](#)].
- [18] V. Desjacques *et al.*, *Mon. Not. R. Astron. Soc.* **451**, 4460 (2015), [[arXiv:1503.05589](#)].
- [19] D. J. Fixsen, *Astrophys. J.* **707**, 916 (2009), [[arXiv:0911.1955](#)].
- [20] J. C. Mather *et al.*, *Astrophys. J.* **512**, 511 (1999), [[arXiv:astro-ph/9810373](#)].
- [21] Y. Hoffman, H. M. Courtois and R. B. Tully, *Mon. Not. R. Astron. Soc.* **449**, 4494 (2015), [[arXiv:1503.05422](#)].
- [22] D. J. Fixsen *et al.*, *Astrophys. J.* **420**, 445 (1994).
- [23] Planck Collab. 2013 Results XXVII, *Astron. Astrophys.* **571**, A27 (2014), [[arXiv:1303.5087](#)].
- [24] S. Seager, D. D. Sasselov and D. Scott, *Astrophys. J. Supp.* **128**, 407 (2000), [[arXiv:astro-ph/9912182](#)].
- [25] L. Knox, *Phys. Rev. D* **52**, 4307 (1995), [[arXiv:astro-ph/9504054](#)].
- [26] N. Bartolo *et al.*, *Phys. Rep.* **402**, 103 (2004), [[arXiv:astro-ph/0406398](#)].
- [27] Planck Collab. 2013 Results XXIV, *Astron. Astrophys.* **571**, A24 (2014), [[arXiv:1303.5084](#)].
- [28] C. L. Bennett *et al.*, *Astrophys. J. Supp.* **192**, 17 (2011), [[arXiv:1001.4758](#)].
- [29] Planck Collab. 2013 Results XXIII, *Astron. Astrophys.* **571**, A23 (2014), [[arXiv:1303.5083](#)].
- [30] Planck Collab. 2018 Results X, *Astron. Astrophys.* **641**, A10 (2020), [[arXiv:1807.06211](#)].
- [31] A. R. Liddle and D. H. Lyth, *Cosmological Inflation and Large-Scale Structure*, Cambridge University Press, Cambridge (2000).
- [32] U. Seljak and M. Zaldarriaga, *Astrophys. J.* **469**, 437 (1996), [[arXiv:astro-ph/9603033](#)].

- [33] A. Lewis, A. Challinor and A. Lasenby, *Astrophys. J.* **538**, 473 (2000), [[arXiv:astro-ph/9911177](#)].
- [34] D. Blas, J. Lesgourgues and T. Tram, *J. Cosmology Astropart. Phys.* **7**, 034 (2011), [[arXiv:1104.2933](#)].
- [35] U. Seljak *et al.*, *Phys. Rev.* **D68**, 083507 (2003), [[arXiv:astro-ph/0306052](#)].
- [36] R. K. Sachs and A. M. Wolfe, *Astrophys. J.* **147**, 73 (1967).
- [37] R. G. Crittenden and N. Turok, *Phys. Rev. Lett.* **76**, 575 (1996), [[arXiv:astro-ph/9510072](#)]; Planck Collab. 2015 Results XXI, *Astron. Astrophys.* **594**, A21 (2016), [[arXiv:1502.01595](#)].
- [38] W. Hu *et al.*, *Phys. Rev.* **D59**, 2, 023512 (1998), [[arXiv:astro-ph/9806362](#)].
- [39] W. Hu, N. Sugiyama and J. Silk, *Nature* **386**, 37 (1997), [[arXiv:astro-ph/9604166](#)].
- [40] P. J. E. Peebles and J. T. Yu, *Astrophys. J.* **162**, 815 (1970); Sunyaev, R. A. and Zeldovich, Ya. B., *Astron. Astrophys. Supp.* **7**, 3 (1970).
- [41] D. Scott, J. Silk and M. White, *Science* **268**, 829 (1995), [[arXiv:astro-ph/9505015](#)].
- [42] D. J. Eisenstein, *New Astron. Rev.* **49**, 360 (2005).
- [43] J. Silk, *Astrophys. J.* **151**, 459 (1968).
- [44] M. Zaldarriaga and U. Seljak, *Phys. Rev.* **D58**, 023003 (1998), [[arXiv:astro-ph/9803150](#)].
- [45] Planck Collab. 2013 Result XVII, *Astron. Astrophys.* **571**, A17 (2014), [[arXiv:1303.5077](#)].
- [46] M. Kaplinghat, L. Knox and Y.-S. Song, *Phys. Rev. Lett.* **91**, 24, 241301 (2003), [[arXiv:astro-ph/0303344](#)].
- [47] Planck Collab. 2013 Results XV, *Astron. Astrophys.* **571**, A15 (2014), [[arXiv:1303.5075](#)].
- [48] Planck Collab. 2018 Results V, *Astron. Astrophys.* **641**, A5 (2020), [[arXiv:1907.12875](#)].
- [49] S. Das *et al.*, *J. Cosmology Astropart. Phys.* **4**, 014 (2014), [[arXiv:1301.1037](#)].
- [50] K. T. Story *et al.*, *Astrophys. J.* **779**, 86 (2013), [[arXiv:1210.7231](#)].
- [51] W. Hu and M. White, *New Astron.* **2**, 323 (1997), [[arXiv:astro-ph/9706147](#)].
- [52] W. Hu and M. J. White, *Phys. Rev.* **D56**, 596 (1997), [[arXiv:astro-ph/9702170](#)].
- [53] M. Zaldarriaga and U. Seljak, *Phys. Rev.* **D55**, 1830 (1997), [[arXiv:astro-ph/9609170](#)]; M. Kamionkowski, A. Kosowsky and A. Stebbins, *Phys. Rev.* **D55**, 7368 (1997), [[arXiv:astro-ph/9611125](#)].
- [54] J. M. Kovac *et al.*, *Nature* **420**, 772 (2002), [[arXiv:astro-ph/0209478](#)].
- [55] D. Larson *et al.*, *Astrophys. J. Supp.* **192**, 16 (2011), [[arXiv:1001.4635](#)].
- [56] Keck Array and BICEP2 Collabs. V, *Astrophys. J.* **811**, 126 (2015), [[arXiv:1502.00643](#)].
- [57] S. K. Choi *et al.*, *J. Cosmology Astropart. Phys.* **2020**, 12, 045 (2020), [[arXiv:2007.07289](#)].
- [58] A. T. Crites *et al.*, *Astrophys. J.* **805**, 36 (2015), [[arXiv:1411.1042](#)].
- [59] L. Balkenhol *et al.*, *Phys. Rev.* **D108**, 2, 023510 (2023), [[arXiv:2212.05642](#)].
- [60] Planck Collab. 2018 Results VII, *Astron. Astrophys.* **641**, A7 (2020), [[arXiv:1906.02552](#)].
- [61] M. Tristram *et al.*, *Astron. Astrophys.* **647**, A128 (2021), [[arXiv:2010.01139](#)].
- [62] D. Hanson *et al.*, *Phys. Rev. Lett.* **111**, 14, 141301 (2013), [[arXiv:1307.5830](#)].
- [63] BICEP2 Collab., *Phys. Rev. Lett.* **112**, 24, 241101 (2014), [[arXiv:1403.3985](#)].
- [64] BICEP2/Keck and Planck Collabs., *Phys. Rev. Lett.* **114**, 10, 101301 (2015), [[arXiv:1502.00612](#)].
- [65] BICEP2 and Keck Array Collab., *Phys. Rev. Lett.* **121**, 22, 221301 (2018), [[arXiv:1810.05216](#)].

- [66] BICEP/Keck Collab., *Phys. Rev. Lett.* **127**, 151301 (2021), [[arXiv:2110.00483](#)].
- [67] POLARBEAR Collab., *Astrophys. J.* **848**, 121 (2017), [[arXiv:1705.02907](#)].
- [68] J. T. Sayre *et al.*, *Phys. Rev.* **D101**, 12, 122003 (2020), [[arXiv:1910.05748](#)].
- [69] Planck Collab. 2015 Results XV, *Astron. Astrophys.* **594**, A15 (2016), [[arXiv:1502.01591](#)].
- [70] A. van Engelen *et al.*, *Astrophys. J.* **808**, 7 (2015), [[arXiv:1412.0626](#)].
- [71] P. Ade *et al.* (Simons Observatory Collab.), *J. Cosmology Astropart. Phys.* **2019**, 2, 056 (2019), [[arXiv:1808.07445](#)].
- [72] K. N. Abazajian *et al.*, ArXiv e-prints (2016), [[arXiv:1610.02743](#)].
- [73] LiteBIRD Collaboration, *Progress of Theoretical and Experimental Physics* **2023**, 4, 042F01 (2023), [[arXiv:2202.02773](#)].
- [74] Planck Collab. 2018 Results VIII, *Astron. Astrophys.* **641**, A8 (2020), [[arXiv:1807.06210](#)].
- [75] F. J. Qu *et al.*, arXiv e-prints [arXiv:2304.05202](#) (2023), [[arXiv:2304.05202](#)].
- [76] W. L. K. Wu *et al.*, *Astrophys. J.* **884**, 1, 70 (2019), [[arXiv:1905.05777](#)].
- [77] D. Scott *et al.*, *J. Cosmology Astropart. Phys.* **2016**, 6, 046 (2016), [[arXiv:1603.03550](#)].
- [78] L. Knox and Y.-S. Song, *Phys. Rev. Lett.* **89**, 1, 011303 (2002), [[arXiv:astro-ph/0202286](#)]; M. Kesden, A. Cooray and M. Kamionkowski, *Phys. Rev. Lett.* **89**, 011304 (2002), [[arXiv:astro-ph/0202434](#)]; C. M. Hirata and U. Seljak, *Phys. Rev.* **D68**, 8, 083002 (2003), [[arXiv:astro-ph/0306354](#)].
- [79] Planck Collab. 2013 Results XII, *Astron. Astrophys.* **571**, A12 (2014), [[arXiv:1303.5072](#)]; Planck Collab. 2015 Results X, *Astron. Astrophys.* **594**, A10 (2016), [[arXiv:1502.01588](#)]; Planck Collab. 2018 Results IV, *Astron. Astrophys.* **641**, A4 (2020), [[arXiv:1807.06208](#)].
- [80] B. Gold *et al.*, *Astrophys. J. Supp.* **192**, 15 (2011), [[arXiv:1001.4555](#)].
- [81] Planck Collab. Interm. Results XXX, *Astron. Astrophys.* **586**, A133 (2016), [[arXiv:1409.5738](#)].
- [82] M. Millea *et al.*, *Astrophys. J.* **746**, 4 (2012), [[arXiv:1102.5195](#)].
- [83] Sunyaev, R. A. and Zeldovich, Ya. B., *Ann. Rev. Astron. Astrophys.* **18**, 537 (1980).
- [84] R. Williamson *et al.*, *Astrophys. J.* **738**, 139 (2011), [[arXiv:1101.1290](#)].
- [85] M. Hilton *et al.*, *Astrophys. J. Supp.* **253**, 1, 3 (2021), [[arXiv:2009.11043](#)].
- [86] Planck Collab. Early Results VIII, *Astron. Astrophys.* **536**, A8 (2011), [[arXiv:1101.2024](#)].
- [87] Planck Collab. 2013 Results XX, *Astron. Astrophys.* **571**, A20 (2014), [[arXiv:1303.5080](#)].
- [88] T. de Haan *et al.*, *Astrophys. J.* **832**, 95 (2016), [[arXiv:1603.06522](#)].
- [89] Planck Collab. 2018 Results IX, *Astron. Astrophys.* **641**, A9 (2020), [[arXiv:1905.05697](#)].
- [90] Planck Collab. 2015 Results XVI, *Astron. Astrophys.* **594**, A16 (2016), [[arXiv:1506.07135](#)].
- [91] Planck Collab. 2013 Results XXII, *Astron. Astrophys.* **571**, A22 (2014), [[arXiv:1303.5082](#)]; Planck Collab. 2015 Results XX, *Astron. Astrophys.* **594**, A20 (2016), [[arXiv:1502.02114](#)].
- [92] Planck Collab. 2015 Results XIV, *Astron. Astrophys.* **594**, A14 (2016), [[arXiv:1502.01590](#)].
- [93] Planck Collab. Interm. Results XLVI, *Astron. Astrophys.* **596**, A107 (2016), [[arXiv:1605.02985](#)].
- [94] X. Fan, C. L. Carilli and B. Keating, *Ann. Rev. Astron. Astrophys.* **44**, 415 (2006), [[arXiv:astro-ph/0602375](#)].
- [95] C. A. Mason *et al.*, *Astrophys. J.* **856**, 1, 2 (2018), [[arXiv:1709.05356](#)].

- [96] Planck Collab. Interm. Results XLIX, *Astron. Astrophys.* **596**, A110 (2016), [[arXiv:1605.08633](#)]; E. Komatsu, *Nature Reviews Physics* **4**, 7, 452 (2022), [[arXiv:2202.13919](#)].
- [97] M. Kamionkowski and A. Kosowsky, *Ann. Rev. Nucl. Part. Sci.* **49**, 77 (1999), [[arXiv:astro-ph/9904108](#)].
- [98] Planck Collab. 2015 Results XIX, *Astron. Astrophys.* **594**, A19 (2016), [[arXiv:1502.01594](#)].
- [99] Planck Collab. Interm. Results XXIV, *Astron. Astrophys.* **580**, A22 (2015), [[arXiv:1406.7482](#)].